Photoacoustic imaging of living mouse brain vasculature using hollow gold nanospheres

Wei Lu [a], Qian Huang [a], Geng Ku [b], Xiaoxia Wen [a], Min Zhou [a], Dmitry Guzatov [c,1], Peter Brecht [c], Richard Su [c], Alexander Oraevsky [c], Lihong V. Wang [b], Chun Li [a,*]

[a] Department of Experimental Diagnostic Imaging, Unit 59, The University of Texas M. D. Anderson Cancer Center, 1515 Holcombe Boulevard, Houston, TX 77030, USA
[b] Optical Imaging Laboratory, Department of Biomedical Engineering, Washington University, St. Louis, MO 63130, USA
[c] Fairway Medical Technologies, Inc., Houston, TX 77099, USA

ARTICLE INFO

ABSTRACT

Photoacoustic tomography (PAT) also referred to as optoacoustic tomography (OAT) is a hybrid imaging modality that employs nonionizing optical radiation and ultrasonic detection. Here, we describe the application of a new class of optical contrast agents based on mesoscopic hollow gold nanospheres (HAuNS) to PAT. HAuNS are $\sim$40 nm in diameter with a hollow interior and consist of a thin gold wall. They display strong resonance absorption tuned to the near-infrared (NIR) range, with an absorption peak at 800 nm, whose photoacoustic efficiency is significantly greater than that of blood. Following surface conjugation with thiolated poly(ethylene glycol), the pegylated HAuNS (PEG-HAuNS) had distribution and elimination half-lives of 1.38 ± 0.38 and 71.82 ± 30.46 h, respectively. Compared with PAT images based on the intrinsic optical contrast in nude mice, the PAT images acquired within 2 h after intravenous administration of PEG-HAuNS showed the brain vasculature with greater clarity and detail. The image depicted brain blood vessels as small as $\sim$100 μm in diameter using PEG-HAuNS as contrast agents. Preliminary results showed no acute toxicity to the liver, spleen, or kidneys in mice following a single imaging dose of PEG-HAuNS. Our results indicate that PEG-HAuNS are promising contrast agents for PAT, with high spatial resolution and enhanced sensitivity.

© 2009 Elsevier Ltd. All rights reserved.

1. Introduction

Noninvasive molecular and functional imaging techniques show promise for detecting and monitoring various physiological and pathological conditions in animals and, ultimately, humans. Among these imaging modalities, photoacoustic imaging offers higher spatial resolution and allows deeper tissues to be imaged than most optical imaging techniques [1–8]. Photoacoustic tomography (PAT) referred to as optoacoustic tomography (OAT) is a hybrid, nonionizing imaging modality that combines the merits of both optical and ultrasonic imaging methods [6]. PAT detects absorbed photons ultrasonically through the photoacoustic effect: a short-pulsed laser irradiates biological tissues and induces wideband ultrasonic waves (photoacoustic waves) as a result of transient thermoelastic expansion [8]. Owing to the optical absorption of hemoglobin, PAT has been successfully applied to the visualization of different structures in biological tissues, especially to imaging of the cerebral cortex in small animals [9,10], human blood vessels [10,11], microvasculature of tumors [4,12] and quantifying oxygen hemoglobin saturation in tumors [2,5,9,13].

PAT is capable of monitoring exogenous optical contrast agents with high sensitivity and specificity [5,11,14]. Optical contrast allowed spectroscopic separation of signal contributions from multiple optical absorbers such as oxyhemoglobin, deoxyhemoglobin, and molecular contrast agents, thus enabling simultaneous molecular and functional imaging [5]. Recently, gold nanoparticles such as gold nanoshells [7], nanocages [15,16], nanorods [17–23], and nanobeacons [24], as well as carbon nanotubes [25–27], have been employed as molecular contrast enhancement agents in the near-infrared (NIR) range, where intrinsic optical absorption in tissue is minimal and penetration is optimal [28]. These gold nanoparticles can generate greater photoacoustic signals due to light excitation in the NIR spectral region, where the signal ratio of gold nanoparticles to hemoglobin is higher, thus showing greater contrast to endogenous chromophores [14,26]. Moreover, the gold nanoparticles are not susceptible to photobleaching, a problem commonly associated with the

---

* Corresponding author. Tel.: +1 713 792 5182; fax: +1 713 794 5456.
  E-mail address: cli@mdanderson.org (C. Li).
[1] Present address: Grodno State University, Grodno, Belarus.

use of organic dyes. These nanoparticles showed enhanced photoacoustic mapping of cerebral vasculature [7,15], sentinel lymph node [16,18,27] and tumor in vivo [25,26], joint tissue ex vivo [29], and macrophages in atherosclerotic plaques [30]. PAT also can noninvasively image the progressive extravasation of gold nanoshells through solid tumor vasculature in vivo [31]. In addition, gadolinium (Gd)-doped, gold-speckled silica nanoparticles were synthesized as multimodal nanoparticulate contrast agents for noninvasive imaging using both magnetic resonance imaging (MRI) and PAT [32].

Hollow gold nanospheres (HAuNS) have the unique combination of small size (outer diameter, 40–50 nm), spherical shape, and a hollow interior that results from their highly uniform structure [33–35]. The HAuNS have a strong and precisely tunable absorption band peaked at ~800 nm and are coated with polyethylene glycol (PEG, MW 5000) to increase their blood circulation half-life. The purpose of this study was to evaluate the use of these HAuNS as a new molecular contrast agent for PAT. The accuracy of PAT with pegylated HAuNS (PEG-HAuNS) of mouse brain vasculature was confirmed through histological analysis. The pharmacokinetics, biodistribution, and acute toxicity of PEG-HAuNS were assessed to provide preliminary data for future translation in clinical applications.

2. Materials and methods

2.1. Materials

Biotinylated secondary antibody, straptavidin-horseradish peroxidase (straptavidin-HRP), 3,3′-diaminobensidine (DAB), hematoxylin, luciferin, and 4% paraformaldehyde were purchased from Fisher Scientific (Waltham, MA). Rat anti-mouse CD31 monoclonal antibody was purchased from Millipore (Billerica, MA). Alexa Fluor 594-tagged goat anti-rat IgG and RPMI-1640 phenol red free cell culture medium were purchased from Invitrogen (Carlsbad, CA). Rat anti-mouse CD 68 antibody was obtained from AbD Serotec (Raleigh, NC). Isoflurane was obtained from Baxter (Deerfield, IL). Methoxy-polyethylene glycol-SH (MPEG-SH, MW = 5000), 3-(4,5-dimethylthiazol-2-yl)-2,5-diphenyltetrazolium bromide (MTT)-based in vitro toxicity assay kit, 10% buffered formalin-saline, and all the other solvents were purchased from Sigma–Aldrich Chemical (St. Louis, MO). ^{111}InCl$_3$ was purchased from Perkin–Elmer (Waltham, MA). All the chemicals and solvents were at least ACS grade and were used without further purification. Human umbilical vein endothelial cells (HUVECs) were obtained from the American Type Culture Collection (Manassas, VA).

2.2. Synthesis of PEG-HAuNS

HAuNS were synthesized according to our previously published methods [33,34]. For the conjugating reaction, about 0.5 mg of MPEG-SH was added into the HAuNS solution (8.5×10^{12} nanoparticles in 4.0 mL water). The solution was stirred overnight at room temperature and then centrifuged at 7000 rpm for 15 min. The PEG-HAuNS were washed three times with water and collected for further characterization.

2.3. Calculation of extinction spectra of PEG-HAuNS

In the case of metallic nanoshells, when the real part of a dielectric permittivity of a nanoshell has a negative value, the spectra of optical absorption and scattering have specific resonance peaks, which correspond to the excitation of surface plasmons in nanoshells [36]. To calculate these spectra of absorption and scattering of light in a gold nanoshell with a water core, we assumed that the incident light was a plane wave propagating along the z axis of a Cartesian system of coordinates. This assumption allowed us to apply standard Mie theory [37] to our calculations, as well as to use the following expressions for absorption (σ_{abs}) and scattering (σ_{scat}) cross-sections [38]:

$$
\begin{aligned}
\sigma_{scat} &= \frac{2\pi\sqrt{\varepsilon_m}}{k_m^2}\sum_{n=1}^{\infty}(2n+1)\left(|a_n|^2+|b_n|^2\right), \\
\sigma_{abs} &= \frac{2\pi\sqrt{\varepsilon_m}}{k_m^2}\sum_{n=1}^{\infty}(2n+1)\mathrm{Re}(a_n+b_n) - \sigma_{scat},
\end{aligned}
\tag{1}
$$

where $\sqrt{\varepsilon_m}$ is a dielectric constant of a host medium, k_m is a wave number of an incident plane wave (in a host medium), and a_n, b_n are the Mie coefficients of scattered field. It should be noted here that in the cross-sections of Eq. (1), the physical meaning of absorbed and scattered power was divided by the energy density of the incident laser radiation in a vacuum. To calculate the Mie coefficients,

we used boundary conditions for the Maxwell equations for the considered geometry. In the case of a metal nanoshell with a dielectric core, the Mie coefficients were calculated by using the method described by Kerker [39].

To quantify the photoacoustic contrast enhancement by PEG-HAuNS, a three-dimensional tomographic image was obtained from a quantitatively characterized phantom using a photoacoustic tomography system (Fairway Medical Technologies, Houston, TX). The phantom was made of poly(vinyl-chloride) plastisol (PVCP) with added TiO$_2$ powder for optical scattering and contained 4 embedded tubes with diameter of 0.6 mm filled with 4 different optically absorbing media: aqueous solution of CuSO$_4$ (OD = 2.0), mouse blood (OD = 1.6), aqueous solution of India ink (OD = 0.8) and water suspension of PEG-HAuNS (OD = 0.7). The optical density (OD) per 1 cm distance in each medium was determined using a Vis/NIR spectrophotometer (DU 800, Beckman, CA). The phantom was illuminated with 300 ns long pulses of an Alexandrite laser operating at the wavelength of 755 nm. The optical fluence incident on the phantom surface was approximately 10 mJ/cm^2, so that the effective optical fluence incident in the tubes was about 1 mJ/cm^2. The image brightness in the location of each tube was measured.

2.4. PAT experimental setup

The setup for PAT of the mouse brain was made in accordance with previous reports [7,15]. A Q-switched Nd:YAG laser (LS-2137/2, LOTIS TII, Minsk, Belarus) and pumped tunable Ti:sapphire laser (LT-2211A, LOTIS TII, Minsk, Belarus) were employed to excite photoacoustic signals. The lasers provided a pulse duration of less than 15 ns, pulse repetition rate of 10 Hz, and wavelength of 800 nm. The incident energy density of the laser beam was controlled to be less than 10 mJ/cm^2 on the surface of the mouse head. An unfocused ultrasonic transducer (V323, 63.5 mm in diameter; Panametrics, Waltham, MA) with a central frequency of 2.25 MHz and a −6 dB bandwidth of about 70% was used to detect the ultrasound signals. Male nude mice (8–10 weeks old; Charles River Laboratories, Wilmington, MA) were used for the imaging experiments. All animal studies ($n = 3$) were carried out in accordance with institutional guidelines. The mice were anesthetized through the inhalation of a mixture of O$_2$ and isoflurane during the whole experiment. The mouse was set on a homemade mount so that its head protruded into the water tank filled with water through a hole in the tank's bottom. The hole was sealed with a piece of polyethylene film, and the head of the mouse was in direct contact with the film but not with water in the tank. Ultrasonic coupling gel was applied to the surface of the mouse's head. The photoacoustic signals detected by the ultrasonic transducer were amplified (5072PR; Olympus, Waltham, MA) and then recorded by a data acquisition card (Compuscope 14 200; Gage Applied, Lockport, IL) installed in the computer (Precision PWS 490; Dell, Round Rock, TX). The photoacoustic images were reconstructed through a modified back-projection algorithm [40].

One PAT scan was performed before the injection of the contrast agent. Afterwards, PEG-HAuNS (about 2.5×10^{11}) were injected into the mouse tail vein. PAT scanning started at 5, 15, 30, 60, 90, and 120 min, respectively, after dosing. After data acquisition, the mice were sacrificed using CO$_2$. Open-skull surgery was performed to photograph the cerebral cortex. The mouse brain was embedded in Tissue Tek O.C.T. compound® (Sakura, Torrance, CA) for frozen sectioning, and immuno-fluorescence staining was performed on brain tissue slices.

2.5. Immunofluorescence analysis

The mouse brain frozen sections were fixed with 4% paraformaldehyde for 15 min at room temperature. After being washed with PBS, the slices were incubated with 10% goat serum for 30 min at 37 °C and then subjected to rat anti-mouse CD31 monoclonal antibody (1:100) at 4 °C overnight. Alexa Fluor 594-tagged goat anti-rat IgG (1:750) was applied as the secondary antibody for 1 h at room temperature. The slices were examined by fluorescence microscopy (Zeiss Axio Observer.Z1, Carl Zeiss MicroImaging GmbH, Göttingen, Germany). HAuNS nanoparticles were detected on the basis of their light scattering under the dark field.

2.6. Pharmacokinetics and biodistribution study

A chelation agent, S-2-(4-[5-(1,2)dithiolane-3-pentanamide]benzyl)-diethyl-enetriamine pentaacetic acid (DTPA-TA), was synthesized and conjugated to the surface of HAuNS according to previous reported procedures [34,41]. Briefly, for conjugation of the radiometal chelator to the nanoparticles, DTPA-TA (1 mg/mL, 10 μL) was mixed with a 1-mL aqueous solution of HAuNS (1×10^{13} particles/mL) for 4 h at room temperature. This was followed by conjugation of PEG-SH to the nanoparticles according to the above described procedures. For radiolabeling, aliquots of PEG-HAuNS(DTPA) (1×10^{13} particles/mL, 0.5 mL) in 0.1 M sodium acetate solution (pH 5.5) were mixed with an aqueous solution of ^{111}InCl$_3$ (~1 mCi) for 30 min. The radiolabeled HAuNS were then purified by centrifugation at 8000 rpm for 5 min and washed three times with PBS. The radiolabeling efficiency was >99%, and radiolabeled nanoparticles were stable in full mouse serum [34].

For pharmacokinetic analysis, seven nude mice were intravenously injected with ^{111}In-labeled PEG-HAuNS (~50 μCi/mouse), and blood samples were collected from the tail vein at predetermined time points. The animals were euthanized by

CO_2 exposure at the end of the study. For the biodistribution study, 14 mice were given the same amount of radiolabeled PEG-HAuNS ($\sim$50 μCi/mouse). The mice were divided into two groups ($n = 7$) and sacrificed after 24 h and 168 h (7 days), respectively. The blood, heart, liver, spleen, kidney, lung, stomach, intestine, muscle, bone, and brain were removed and weighed, and radioactivity was measured with a Cobra gamma counter (Packard, Downers Grove, IL). Uptake of ^{111}In-labeled nanoparticles in various organs was calculated as percentage of injected dose per gram of tissue (%ID/g).

2.7. Cytotoxicity assay

The cytotoxicity of PEG-HAuNS was evaluated in HUVECs according to a previously reported method [42]. Following three days of continuous exposure to the nanoparticles, cell viability was measured using an MTT-based *in vitro* toxicology assay kit. The absorbance was measured on a SpectraMax Plus[384] microplate spectrophotometer (Molecular Devices, Sunnyvale, CA), with a test wavelength of 570 nm and a reference wavelength of 630 nm. The percentage of viable cells at each concentration relative to nontreated cells was plotted. Citrate-stabilized gold nanoparticles (AuNP) and cetyltrimethylammonium bromide (CTAB) stable gold nanorods with a particle size of around 40 nm were synthesized according to previous reports and used as controls [42].

In a separate experiment, the intensity of bioluminescence produced by human glioblastoma U87 cells stably transfected with the luciferase gene (U87-TGL, a gift from Dr. Juri Gelovani, The University of Texas M. D. Anderson Cancer Center) was measured to evaluate the cytotoxicity of the nanoparticles. The cells were seeded onto a 96-well plate. After three days' exposure to different concentrations of the above particles, the cells were subjected to luciferin (0.5 mg/mL) in RPMI-1640 phenol red free. The bioluminescent signals were recorded using the Xenogen IVIS-200 Optical In Vivo Imaging System (Caliper Life Sciences, Hopkinton, MA). The luminescent intensity was quantified, and the percentage of the intensity at each concentration relative to that of the nontreated cells was plotted.

2.8. Blood hematology, biochemistry and histology

Fourteen male Swiss mice were randomly divided into two groups ($n = 7$). Each group received an intravenous injection of 2.5×10^{11} PEG-HAuNS or saline. Blood samples were collected on 7 days after nanoparticle injection for hematologic and chemical analysis.

For histological evaluation, portions of the kidney, liver, and spleen collected on day 7 after PEG-HAuNS injection were fixed in 10% buffered formalin-saline at 4 °C overnight and then embedded in paraffin blocks. Tissue sections 5 μm thick were stained with hematoxylin and eosin (H&E). Immunohistochemical analysis was performed using a 1:100 dilution of rat anti-mouse CD68 antibody overnight at 4 °C. Slides were then rinsed and incubated with biotinylated secondary antibody, after which they were incubated with straptavidin-HRP. Slides were developed with DAB and counter-stained with hematoxylin.

2.9. Statistical analysis

The blood pharmacokinetic parameters of the radiotracer were analyzed with a two-compartmental model using WinNonlin 5.0.1 software (Pharsight Corporation, Palo Alto, CA). Student's *t*-test (two tailed, unpaired) was performed to compare serum analysis results between nanoparticle groups and saline controls, and *p* values less than 0.05 were considered statistically significant.

3. Results and discussion

3.1. PEG-HAuNS characterizations

A transmission electron microscopy (TEM) image of PEG-HAuNS shows that the nanoparticles had a mean outer diameter of 43–46 nm and a mean shell thickness of 2–4 nm (Fig. 1A). The
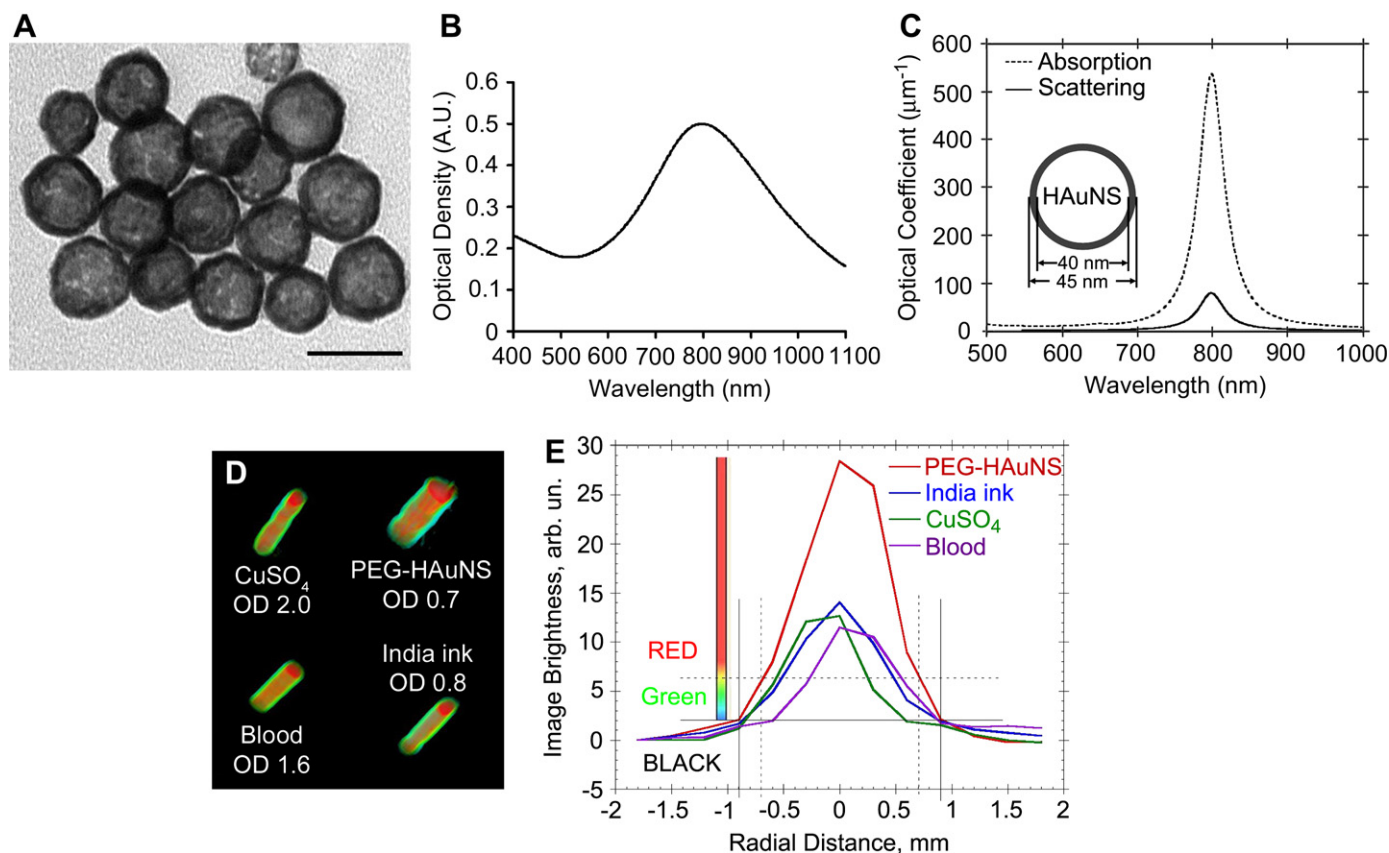

Fig. 1. (A) TEM image of PEG-HAuNS (Bar = 50 nm). The average outer diameter was 45 nm, and thickness of the shell was 2.5 nm. (B) Experimental absorbance spectrum of PEG-HAuNS in water, which peaked at 800 nm. (C) Theoretically calculated absorption and scattering spectra of PEG-HAuNS with water core having dielectric permittivity of 1.77. The inner core radius was 20 nm and gold shell thickness was 2.5 nm, whose values are consistent with those shown in TEM. (D) Tomographic image of a tissue mimicking phantom made of poly(vinyl-chloride) plastisol with embedded four tubes filled with optically absorbing liquid media. (E) Quantitative analysis of the photoacoustic image brightness through the cross-section of each tube from (D). The color scale was designed in three steps: from black to blue/green to red. All tubes with different levels of brightness reflected in the object diameter.

resonance absorbance of these nanoparticles was tuned to peak at 800 nm (Fig. 1B). The optical absorption and scattering coefficients of gold nanospheres (i.e., absorption and scattering cross-sections per unit volume) were calculated (Fig. 1C). Our calculations showed that HAuNS with an outer diameter of 45 nm and shell thickness of 2.5 nm had an extinction spectrum that peaked at 800 nm. The theoretical dimensions of HAuNS matched well with the measured dimensions shown in the TEM image (Fig. 1A). This result validates our calculation, and provides a valuable theoretical approach towards designing HAuNS with absorption and scattering peaks at predetermined wavelengths in the NIR region.

According to the Mie theory and the plasmon resonance theory, the optical absorption coefficient of gold nanoshells increases, while the optical scattering coefficient decreases, with decreasing diameter of the core. The peak wavelength experiences a red shift with decreasing shell thickness. Although the larger size of previously reported silica-cored gold nanoshells (145-nm outer diameter, 10-nm shell thickness) resulted in a much greater extinction value, the extinction of these gold nanoshells was dominated by scattering [15]. The absorption coefficient of the silica-cored gold nanoshells was calculated as 16.9 μm^{-1}, according to its absorption cross-section of 0.027 μm^2 [15]. In contrast, the extinction of our HAuNS was dominated by absorption, owing to their smaller size (Fig. 1C). At 800 nm, the absorption coefficient of HAuNS reached $\sim$540 μm^{-1}, which is 32 times as high as that of silica-cored gold nanoshells. However, the scattering coefficient of HAuNS ($\sim$78 μm^{-1}) is similar as that of silica-cored gold nanoshells ($\sim$75 μm^{-1} calculated from the scattering cross-section of 0.12 μm^2 [15]). Since PAT is an absorption-based technique, this high

absorption coefficient makes our HAuNS an excellent contrast agent for photoacoustic imaging.

To demonstrate utility of PEG-HAuNS as a photoacoustic contrast agent, we acquired a tomographic image of a tissue mimicking phantom made of PVCP with embedded four tubes filled with optically absorbing liquid media (Fig. 1D). The long duration of the laser pulses used in this experiment limited the image resolution to about 1 mm. Thus, the tubes with internal diameters of 0.6 mm are visualized in Fig. 1D as tubes with larger diameters. The diameter of each tube on the image increased with the object brightness (Fig. 1E). The distribution of the photoacoustic image brightness through the cross-section of each tube is shown by bell-shaped curves. Analysis of the image brightness revealed that the photoacoustic image of PEG-HAuNS was brighter than that of whole blood, aqueous solutions of $CuSO_4$ and India ink. Even though blood had optical density 2.3-fold greater than that of PEG-HAuNS in water suspension, the photoacoustic brightness of PEG-HAuNS was 2.5-fold greater than that of blood. This experiment demonstrates that the photoacoustic efficiency of PEG-HAuNS is significantly greater than that of blood.

3.2. Mapping of mouse brain vasculature

PAT images of the cerebral cortex of a mouse before and after a single injection of PEG-HAuNS are presented in Fig. 2. Because of the low intrinsic absorption of oxyhemoglobin and deoxyhemoglobin at 800 nm, the photoacoustic signal was weak, with a low signal-to-noise ratio that showed only large vessels distributed along the mouse brain cortical surface, such as the middle
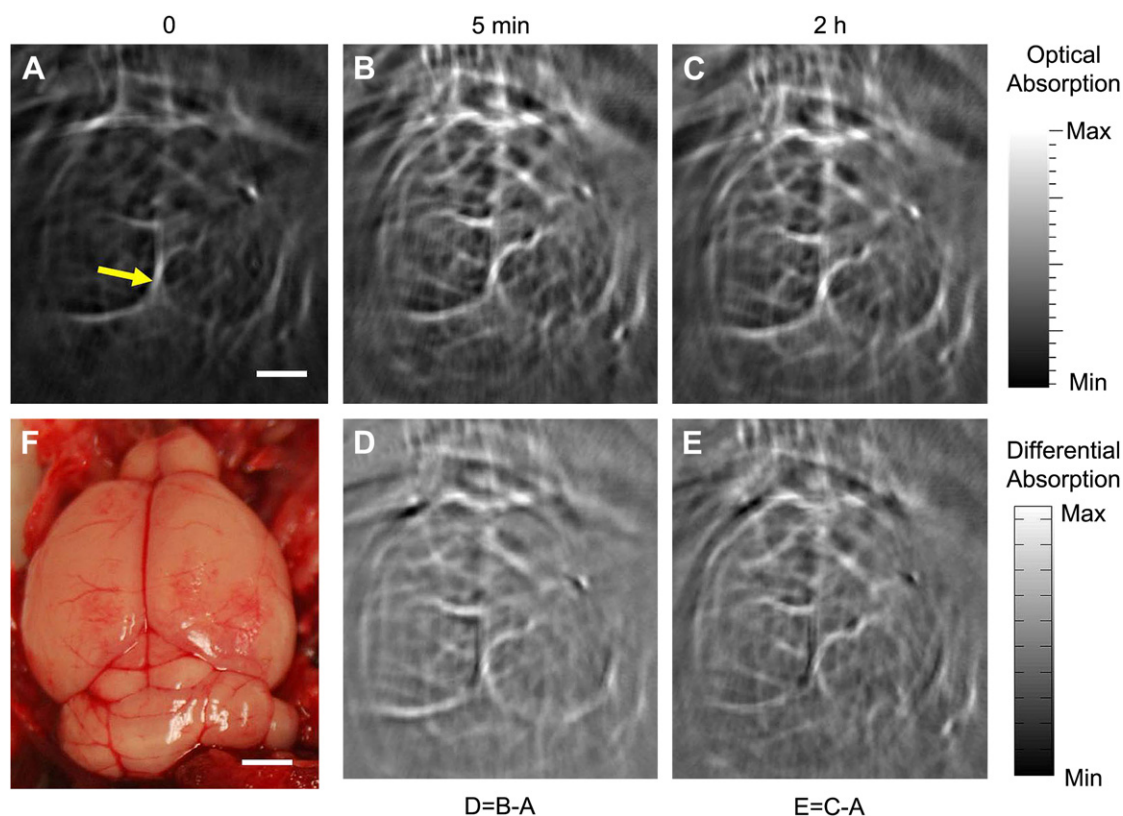

Fig. 2. Noninvasive PAT imaging of a mouse brain *in vivo* employing PEG-HAuNS and NIR light at a wavelength of 800 nm. Photoacoustic image acquired (A) before, (B) 5 min after, and (C) 2 h after the intravenous injection of PEG-HAuNS. (D) and (E) Differential images that were obtained by subtracting the preinjection image from the post-injection images (Image D = Image B − Image A; Image E = Image C − Image A). Arrow, middle cerebral artery. Bar = 2 mm. (F) Open-skull photograph of the mouse brain cortex obtained after the data acquisition for PAT. Bar = 2 mm.
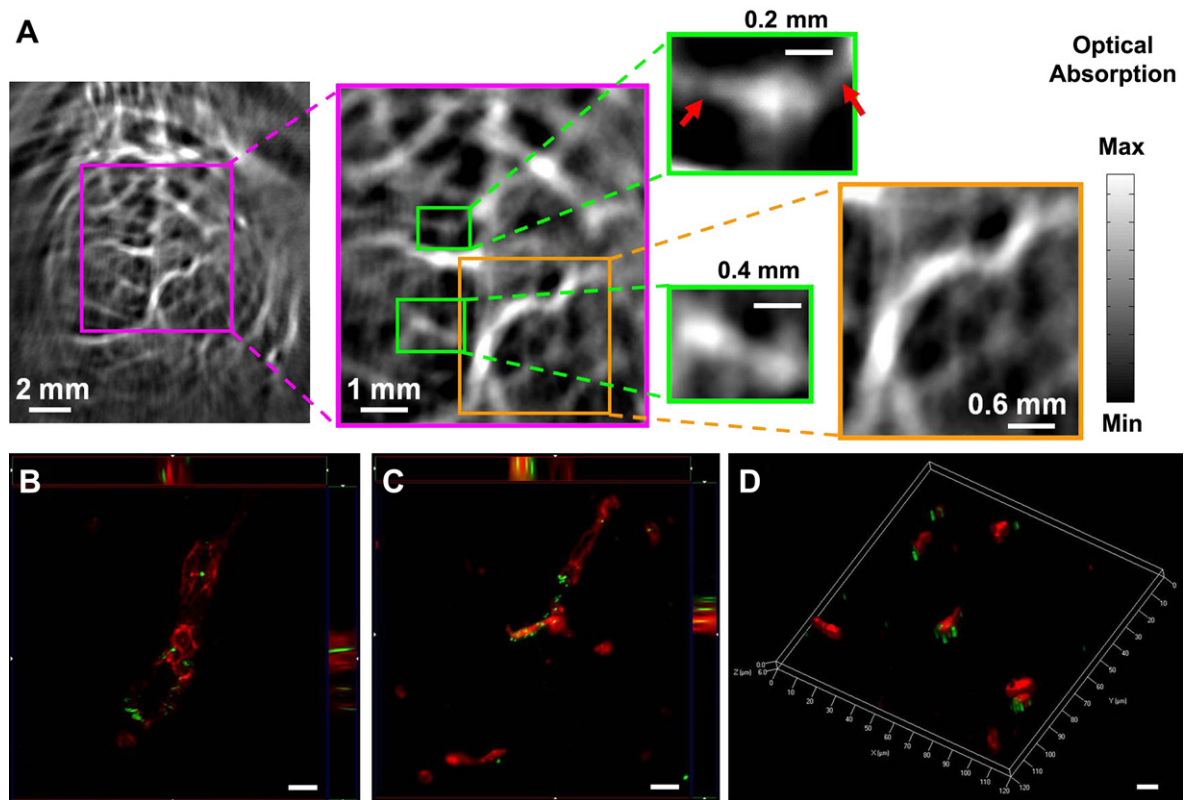
Fig. 3. (A) Enhanced photoacoustic signals revealed clear and detailed structure of large (yellow-framed picture) and small (green-framed picture) blood vessels in the mouse brain at higher magnification 2 h after intravenous injection of PEG-HAuNS. Arrows represent the small blood vessels with a diameter of about 100 μm, which can be seen in the contrast-enhanced images. (B–D) Distribution of PEG-HAuNS in brain vessels 2 h after injection (Bar = 10 μm). Brain vessels were stained with anti-CD31 antibody (red fluorescence), while the scattering signals of gold particles were detected under a dark field (pseudo-green). Z-stack images showed the particles located on the luminal side of brain blood vessels (B and C). In brain capillaries, three-dimensional reconstruction images show that the particles colocalized or stayed adjacent to the brain capillary endothelial cells (D).

cerebral artery (Fig. 2A, arrow). However, 5 min after the injection of PEG-HAuNS, the PAT image revealed the brain vasculature with much greater clarity, especially small blood vessels (Fig. 2B). This enhanced clarity was attributed to the strong photoacoustic signal generated with PEG-HAuNS. The circulating PEG-HAuNS enhanced the contrast between the blood vessels and the brain parenchyma. This is better appreciated in a differential image (Fig. 2D) obtained by subtracting the preinjection image (Fig. 2A) from the post-injection image pixel by pixel (Fig. 2B). At 2 h post-injection, the photoacoustic images remained essentially unchanged, indicating significant amount of PEG-HAuNS circulating in the blood (Fig. 2C and E). The PAT images of the mouse brain matched well with the open-skull anatomical photograph (Fig. 2F).

At higher magnification, PAT revealed not only the structure of large vessels (Fig. 3A, yellow-framed picture) but also small blood vessels (Fig. 3A, green-framed pictures) 2 h after PEG-HAuNS injection. Indeed, brain blood vessels in the superficial cortex as small as ∼100 μm in diameter could be clearly seen (Fig. 3A, arrows).

In order to confirm the distribution of PEG-HAuNS in the brain, the blood vessels were stained with anti-CD31 antibody, while the scattering signal of the gold nanoparticles was detected under a dark field. As shown in Fig. 3B and C, the HAuNS were located on the luminal side of the blood vessels 2 h after intravenous injection. In brain capillaries, most of the nanoparticles colocalized or stayed adjacent to the brain capillary endothelial cells (Fig. 3D). There was no particle extravasation into the brain parenchyma. This was attributed to the blood–brain barrier, which has been shown to impede the penetration of such particles [7]. Therefore, our finding proves that the distribution of high-optical contrast agents in the vasculature can afford clear and enhanced photoacoustic imaging

of brain vessels of live mice with intact skin and skull, as well as a low brain parenchymal background.

The absorption signals from the PAT images acquired at each time point after injection of PEG-HAuNS were integrated and normalized to the signal integration of the preinjection image (Fig. 4, $n = 3$). The highest photoacoustic signal was acquired at 5 min after contrast agent injection and the intensity was 2.3-fold
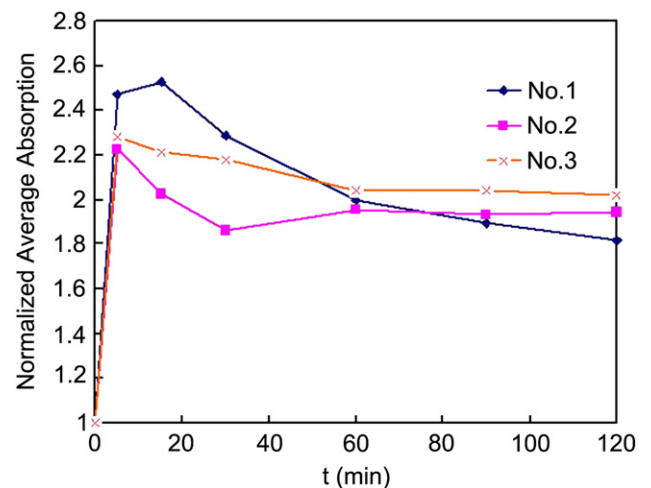

Fig. 4. The integrated absorption calculated from the *in vivo* brain images of three mice at different times following the injection of PEG-HAuNS. The presented values were normalized to that of the integrated absorption of the image obtained before the injection.
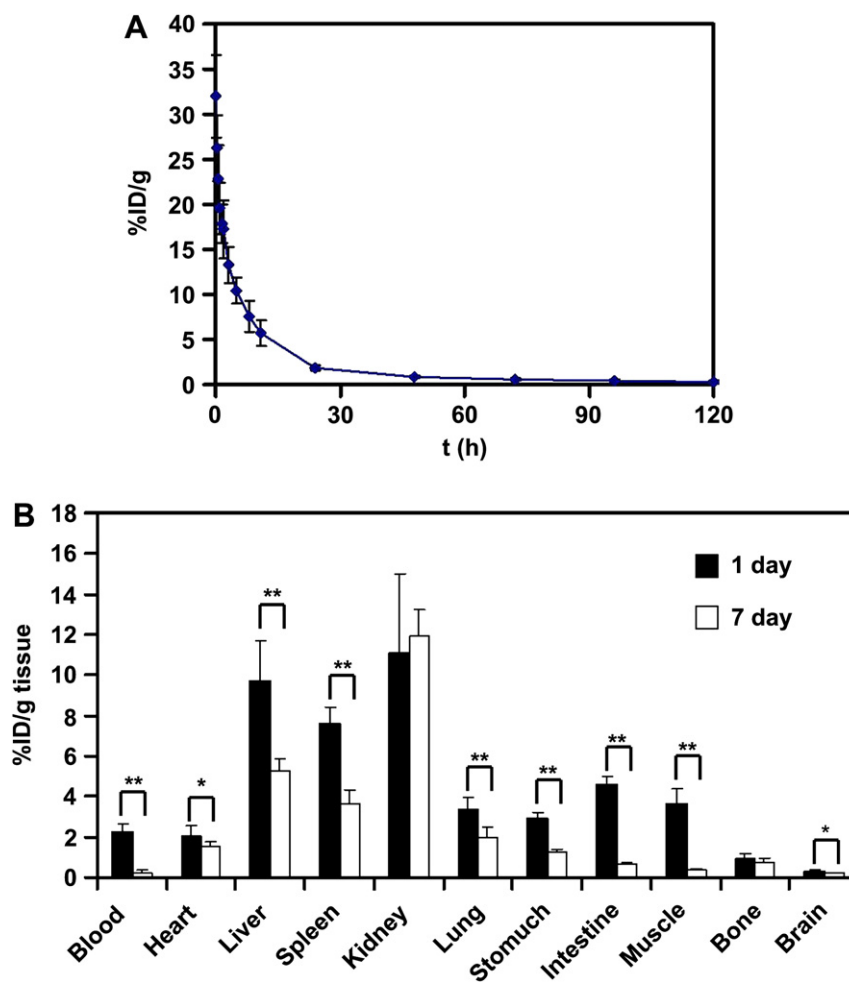
Fig. 5. (A) Blood activity–time profile of PEG-HAuNS(DTPA-^{111}In). The closed circles represent the mean radioactivity expressed as a percentage of the injected dose per gram of blood from seven mice. Data are expressed as mean ± SD. (B) Biodistribution of PEG-HAuNS(DTPA-^{111}In) in nude mice 1 and 7 days after injection. Data were plotted as percentage of injected dose per gram of tissue (% ID/g). Mean ± SD ($n = 7$). *, $p < 0.05$; **, $p < 0.01$.

higher than that of the preinjection value. The absorption enhancement remained high, even after 2 h, with an average increase over the preinjection value of 1.9-fold. This is in accordance with the contrast enhancement seen on post-injection PAT images at 5 min and at 2 h (Fig. 2B and C).

The molar extinction coefficient associated with the optical absorption cross-section of HAuNS is calculated to exceed 1.4×10^{11} M^{-1} cm^{-1} at 800 nm based on Fig. 1C. In comparison, the molar extinction coefficient of hemoglobin is $\sim 1 \times 10^3$ M^{-1} cm^{-1} [43]. As a result, only ~ 20 pM concentration of PEG-HAuNS can give approximately as strong optical absorption as hemoglobin at the typical concentration of 2.3 mM in blood. This gives one an opportunity to inject a relatively small volume of highly concentrated PEG-HAuNS in the blood stream of an animal to enhance the optical absorption of blood in the NIR spectral range. Such enhancement might be even more prominent for targeted tissues of diagnostic interest such as early malignant lesions with relatively low blood content.

3.3. Pharmacokinetics and biodistribution of PEG-HAuNS

Fig. 5A illustrates that the mean blood activity–time profile of ^{111}In-labeled PEG-HAuNS after i.v. injection fit a two-compartment model, with a distribution half-life of 1.38 ± 0.38 h and an elimination half-life of 71.82 ± 30.46 h. Other pharmacokinetic

parameters of PEG-HAuNS after intravenous injection are summarized in Table 1. Fig. 5B shows the tissue distribution of ^{111}In-labeled PEG-HAuNS 1 day and 7 days after injection. The kidneys, liver, and spleen were the major organs taking up a significant amount of HAuNS. Compared with the amount of PEG-HAuNS in tissues 1 day after injection, the uptake of PEG-HAuNS in all organs with the exception of the kidneys and bone significantly decreased at day 7 after injection.

Zhang et al. [41] investigated the size-dependent pharmacokinetics of pegylated solid gold nanoparticles with an average

Table 1
The pharmacokinetic (PK) parameters of ^{111}In-labeled PEGylated HAuNS in nude mice ($n = 7$).

PK parameters	Mean ± SD
$T_{1/2\alpha}$ (h)	1.38 ± 0.38
$T_{1/2\beta}$ (h)	71.82 ± 30.46
$AUC_{(0-\infty)}$ (ID%/mL h)	281.59 ± 45.97
$AUMC_{(0-\infty)}$ (ID%/mL h^2)	14193 ± 8136
MRT (h)	48.93 ± 22.78
CL (mL/h)	0.363 ± 0.058
V_{ss} (mL)	17.3 ± 7.44

AUC = the area under the particle concentration–time curve; AUMC = the area under the first moment of the particle concentration–time curve; MRT = mean residence time; CL = clearance; V_{ss} = volume of distribution at steady−state. ID = injected dose.
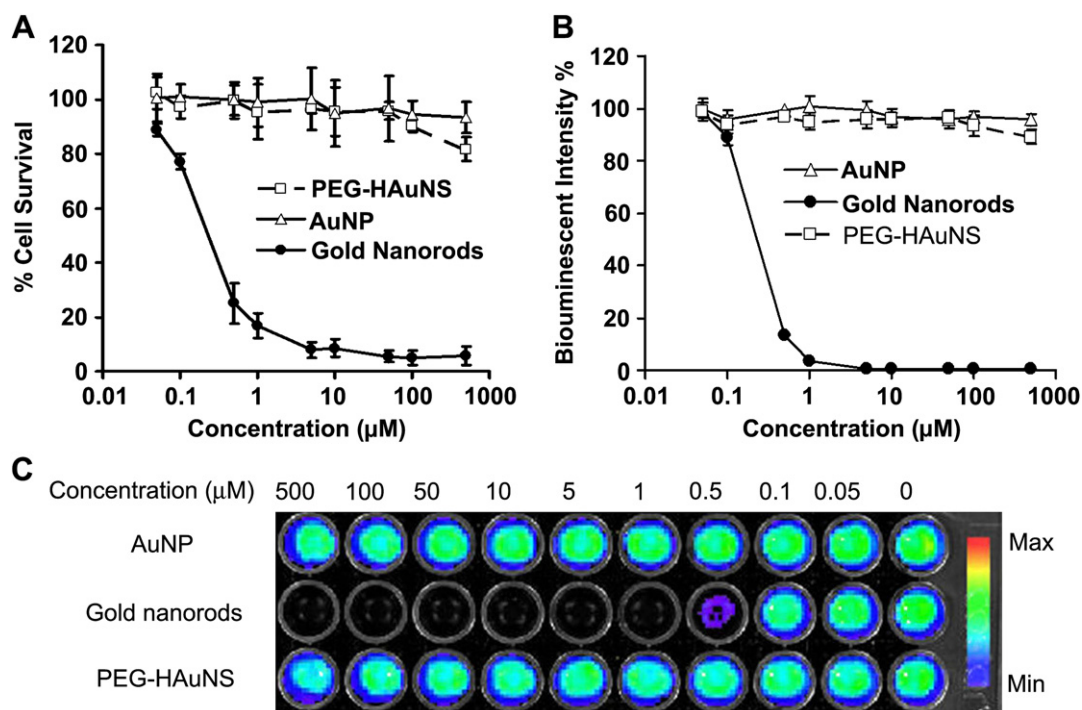
Fig. 6. (A) Viability of HUVEC cells exposed to different nanoparticles. Cell viability was measured by the MTT assay. The data were plotted as the percentage of viable cells compared to untreated controls. (B) Cell viability of U87-TGL cells stably transfected with luciferase and treated with different nanoparticles, which was measured by bioluminescence in addition of luciferin. The data were plotted as the percentage of bioluminescent intensity of surviving cells compared to that of untreated controls. (C) Representative bioluminescent images of U87-TGL cells treated with different kinds of particles at various concentrations.

diameter of less than 100 nm. They found that 20-nm and 40-nm gold nanoparticles were cleared from the blood more slowly and had less uptake in the liver and spleen than 80-nm nanoparticles. The reason might be due to the pegylated smaller particles having higher PEG density than larger particles. The thick PEG layer effectively insulated the gold particles from non-specific binding to plasma proteins, resulting in reduced liver uptake [41]. Our particles with an outer diameter of 45 nm have a similar distribution half-life to that reported for pegylated solid gold nanoparticles 40 nm in diameter (1.38 h vs. 1.32 h [41]). However, the blood elimination half-life of PEG-HAuNS is significantly longer compared to that of pegylated solid gold nanoparticles (71.8 h vs. 10.1 h [41]). One possible explanation is the difference in particle density: HAuNS have lower density than solid Au nanoparticles. Further studies are needed to investigate whether and how particle density may influence the pharmacokinetics and biodistribution of gold nanoparticles.

Table 2
The mouse serum level of biochemical variables at 7 days after intravenous treatment with PEG−HAuNS (1×10^{12} per mouse).

Parameters	Saline	PEG−HAuNS
Creatinine (mg/dl)	<0.20	<0.20
BUN (mg/dl)	25.4 ± 2.7	22.3 ± 4.9
AST (U/L)	105.6 ± 37.8	136.7 ± 72.5
ALT (U/L)	52.8 ± 19.3	54.4 ± 8.6
Alkaline phosphatase (U/L)	126.3 ± 34.5	115.4 ± 24.2
LDH (U/L)	363.3 ± 60.5	345.8 ± 74.5

Values are the means ± SD (ratio to control), $n = 7$. There was no significant difference of the above parameters between PEG−HAuNS group and saline control ($p > 0.05$). BUN, blood urea nitrogen; AST, aspartate aminotransferase; ALT, serum alanine aminotransferase; LDH, lactate dehydrogenase.

3.4. Toxicity evaluation of PEG-HAuNS

Fig. 6A shows the viability of HUVECs following 3 days of continuous exposure to PEG-HAuNS, citrate-stabilized AuNP, or CTAB-capped gold nanorods at different concentrations, as measured by the MTT assay. The PEG-HAuNS and AuNP preparations were not toxic at concentrations up to 500 μM (gold atoms). In contrast, over 90% of HUVECs were killed when the cells were incubated with the CTAB-capped gold nanorod solution at a concentration of 5 μM. The cytotoxicity was also evaluated through the measurement of the function of bioluminescence transformation in human glioblastoma U87 cells stably transfected with the luciferase gene (U87-TGL). Upon addition of luciferin substrate, the decrease in luminescent intensity represented the cytotoxic effects of the different nanoparticles on the cells (Fig. 6B and C). The data suggest that PEG-HAuNS are not inherently toxic to human cells because the HAuNS are made of pure gold and are, therefore, expected to be nontoxic [42]. In comparison, the structure-directing agent CTAB on the surface of gold nanorods was highly toxic to the cells at a concentration as low as ∼10 nM [44].

We further investigated the in vivo toxicity of PEG-HAuNS in mice. Following i.v. injection of a single imaging dose of PEG-HAuNS (2.5×10^{11} particles per mouse), there were no deaths in any of the experimental animal groups during the study period. There was no significant difference in any tested serum biochemical parameters between the mice treated with PEG-HAuNS and those treated with saline 7 days after intravenous injection (Table 2). This indicates that a single PAT imaging dose of PEG-HAuNS does not impair liver or kidney function. H&E staining of the liver, spleen, and kidneys did not show any apparent change in cellular structures 7 days after PEG-HAuNS injection (Fig. 7). To evaluate the acute inflammation caused by the nanoparticles, the tissue sections of liver, spleen, and kidney were stained with CD68, a monocyte/macrophage-specific marker [45]. Because the nanoparticles were
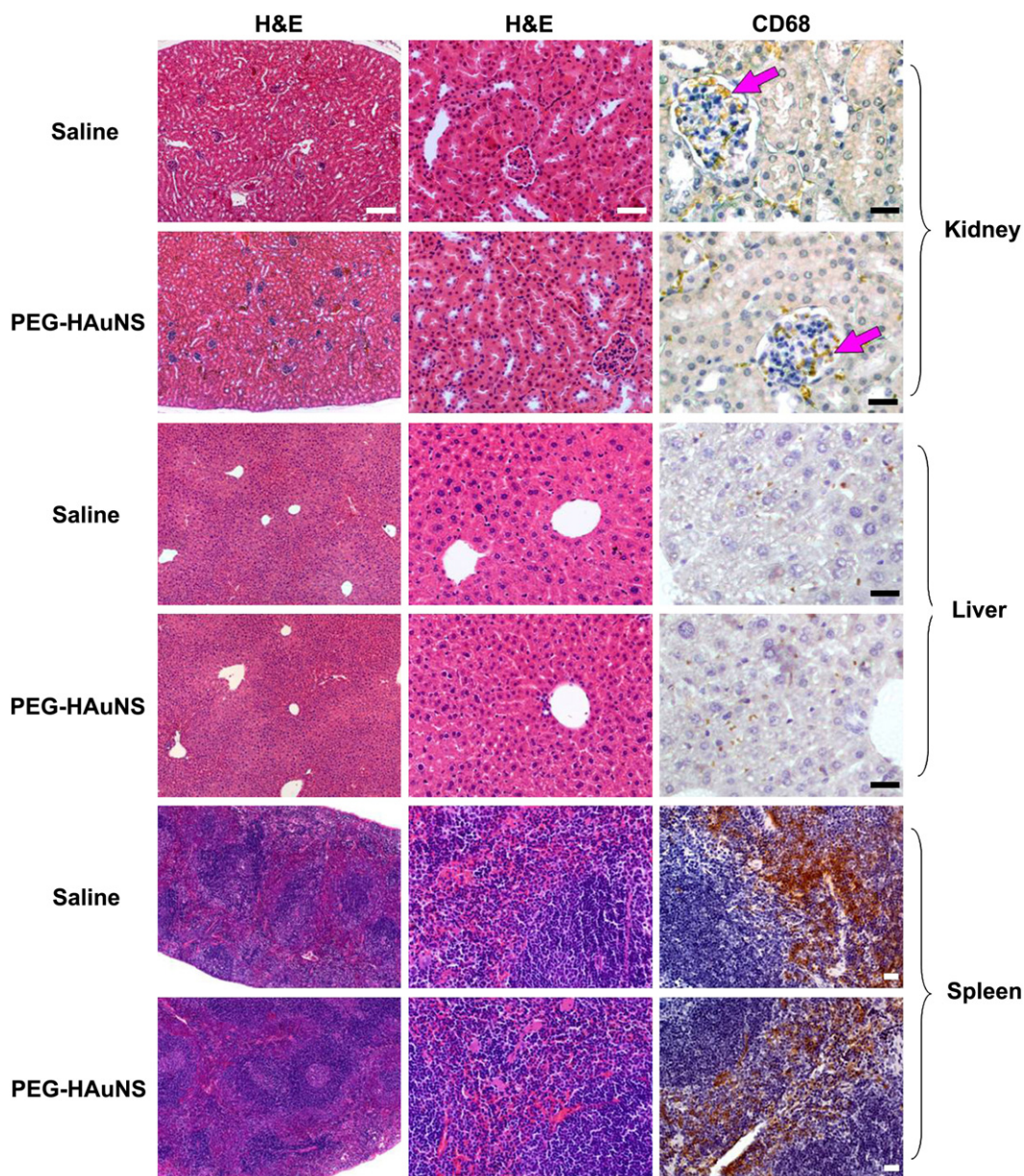
Fig. 7. Histological sections of liver, spleen, and kidney samples collected 7 days following injection of PEG-HAuNS at a dose of 2.5 × 10^{11} particles/mouse. Sections were stained with H&E and CD68 antibody for macrophage visualization. Bars, left = 200 μm; middle = 50 μm; right = 25 μm. Arrows, mesangial cells.

significantly entrapped in the liver and spleen (Fig. 5B), macrophages in the liver (Kupffer cells) and spleen were believed to have taken up the majority of the nanoparticles [46,47]. However, immunohistochemical analysis of hepatic lobules of the liver in mice did not show an increased amount of Kupffer cells (positive staining) 7 days after PEG-HAuNS dosing compared to saline controls (Fig. 7). The macrophages in the marginal zone of the spleen did not significantly increase either. Mesangial cell proliferation with mesangial expansion is commonly observed in glomerulonephritis [48]. Here, though, we did not see a significant change in the amount of positively stained mesangial cells (Fig. 7, arrows) in the kidney in mice injected with PEG-HAuNS compared with saline controls.

It is known that a large portion of intravenously injected nanoparticles are taken up and eliminated by phagocytes, including monocytes in blood circulation and macrophages in tissue [46]. If a non-specific immunoresponse takes place, the monocytes will be recruited from the circulation and infiltrate and develop into macrophages in the inflammatory tissue [45]. Thus, any acute inflammation caused by nanoparticles in vivo could be characterized by an increase in monocytes and macrophages. Previous results have shown that most of the inflammation following nanoparticle injection occurs in the following regions: the hepatic sinusoid, where Kupffer cells capture the blood nanoparticles; the splenic marginal zone, where the nanoparticles are sequestered by macrophages and tightly bound to a reticular meshwork; and the renal corpuscle, where mesangial cells phagocytize and clear the blood nanoparticles [45]. In our study, no such inflammatory reactions occurred in these regions, which is consistent with our in vitro results showing no cytotoxicity against human cell lines. Taken together, our results show that intravenous administration of a single imaging dose of PEG-HAuNS does not cause acute toxicity to

the liver, spleen, or kidneys in mice. Clearly, further work is needed to elucidate the dose–response relationship to acute toxicity. Moreover, the long-term toxic effects of the presence of nanoparticles must be examined before taken into humans.

4. Conclusion

In this study, we evaluated a new nanoparticulate optical contrast agent based on HAuNS for photoacoustic imaging. The particles can be fabricated with surface plasmon resonance tunable at the NIR wavelength ($\sim$800 nm), which allows deeper penetration of laser light and lowers the intrinsic background noise. The photoacoustic efficiency of HAuNS is significantly greater than that of blood. The pegylated HAuNS showed the mouse brain vasculature with greater clarity and more detailed structures, with significant contrast enhancement, than PAT imaging without contrast. Brain blood vessels as small as about 100 μm in diameter could be clearly seen using our PAT system with PEG-HAuNS. Pharmacokinetic results demonstrate that PEG-HAuNS has long circulation in the blood pool. Preliminary toxicity results showed no acute toxicity to the liver, spleen, and kidneys in mice with a single intravenous PAT imaging dose of PEG-HAuNS. Our results indicate that HAuNS are a promising contrast agent for PAT imaging techniques, with high spatial resolution and satisfactory sensitivity based on strong optical absorption in the NIR region. Work on molecular PAT imaging of tumor associated biomarkers using HAuNS as the imaging probe is under way.

Acknowledgements

Appendix

Figures with essential color discrimination. Figs. 2, 4 and 5 in this article are difficult to interpret in black and white. The full color images can be found in the on-line version, at doi:10.1016/j.biomaterials.2009.12.007.

References

[1] Xu MH, Wang LHV. Photoacoustic imaging in biomedicine. Rev Sci Instrum 2006;77(4):041101.
[2] Wang XD, Xie XY, Ku GN, Wang LHV. Noninvasive imaging of hemoglobin concentration and oxygenation in the rat brain using high-resolution photoacoustic tomography. J Biomed Opt 2006;11(2):024015.
[3] Zhang HF, Maslov K, Stoica G, Wang LHV. Functional photoacoustic microscopy for high-resolution and noninvasive in vivo imaging. Nat Biotechnol 2006;24(7):848–51.
[4] Manohar S, Vaartjes SE, van Hespen JCG, Klaase JM, van den Engh FM, Steenbergen W, et al. Initial results of in vivo non-invasive cancer imaging in the human breast using near-infrared photoacoustics. Opt Express 2007;15(19):12277–85.
[5] Li ML, Oh JT, Xie XY, Ku G, Wang W, Li C, et al. Simultaneous molecular and hypoxia imaging of brain tumors in vivo using spectroscopic photoacoustic tomography. Proc IEEE 2008;96(3):481–9.
[6] Oraevsky AA, Jacques SL, Esenaliev RO, Tittel FK. Time-resolved optoacoustic imaging in layered biological tissues. In: Alfano RR, editor. OSA proceedings on advances in optical imaging and photon migration. New York-London: Academic Press; 1994. p. 161–5.
[7] Wang YW, Xie XY, Wang XD, Ku G, Gill KL, O'Neal DP, et al. Photoacoustic tomography of a nanoshell contrast agent in the in vivo rat brain. Nano Lett 2004;4(9):1689–92.
[8] Oraevsky AA, Karabutov AA. Optoacoustic tomography. In: Vo-Dinh T, editor. Biomedical photonics handbook. Boca Raton: CRC Press/Francis and Taylor Group; 2003. p. 1–34.
[9] Wang XD, Pang YJ, Ku G, Xie XY, Stoica G, Wang LHV. Noninvasive laser-induced photoacoustic tomography for structural and functional in vivo imaging of the brain. Nat Biotechnol 2003;21(7):803–6.
[10] Hoelen CGA, de Mul FFM, Pongers R, Dekker A. Three-dimensional photoacoustic imaging of blood vessels in tissue. Opt Lett 1998;23(8):648–50.
[11] Wang XD, Ku G, Wegiel MA, Bornhop DJ, Stoica G, Wang LHV. Noninvasive photoacoustic angiography of animal brains in vivo with near-infrared light and an optical contrast agent. Opt Lett 2004;29(7):730–2.
[12] Ermilov SA, Khamapirad T, Conjusteau A, Leonard MH, Lacewell R, Mehta K, et al. Laser optoacoustic imaging system for detection of breast cancer. J Biomed Opt 2009;14(2):024007.
[13] Lungu GF, Li ML, Xie XY, Wang LHV, Stoica G. In vivo imaging and characterization of hypoxia-induced neovascularization and tumor invasion. Int J Oncol 2007;30(1):45–54.
[14] Copland JA, Eghtedari M, Popov VL, Kotov N, Mamedova N, Motamedi M, et al. Bioconjugated gold nanoparticles as a molecular based contrast agent: implications for imaging of deep tumors using optoacoustic tomography. Mol Imaging Biol 2004;6(5):341–9.
[15] Yang XM, Skrabalak SE, Li ZY, Xia YN, Wang LHV. Photoacoustic tomography of a rat cerebral cortex in vivo with au nanocages as an optical contrast agent. Nano Lett 2007;7(12):3798–802.
[16] Song KH, Kim CH, Cobley CM, Xia YN, Wang LV. Near-infrared gold nanocages as a new class of tracers for photoacoustic sentinel lymph node mapping on a rat model. Nano Lett 2009;9(1):183–8.
[17] Agarwal A, Huang SW, O'Donnell M, Day KC, Day M, Kotov N, et al. Targeted gold nanorod contrast agent for prostate cancer detection by photoacoustic imaging. J Appl Phys 2007;102(6):064701.
[18] Song KH, Kim C, Maslov K, Wang LV. Noninvasive in vivo spectroscopic nanorod-contrast photoacoustic mapping of sentinel lymph nodes. Eur J Radiol 2009;70(2):227–31.
[19] Li PC, Wang CRC, Shieh DB, Wei CW, Liao CK, Poe C, et al. In vivo photoacoustic molecular imaging with simultaneous multiple selective targeting using antibody-conjugated gold nanorods. Opt Express 2008;16(23):18605–15.
[20] Li PC, Wei CW, Liao CK, Chen CD, Pao KC, Wang CRC, et al. Photoacoustic imaging of multiple targets using gold nanorods. IEEE Trans Ultrason Ferroelectr Freq Control 2007;54(8):1642–7.
[21] Kim K, Huang SW, Ashkenazi S, O'Donnell M, Agarwal A, Kotov NA, et al. Photoacoustic imaging of early inflammatory response using gold nanorods. Appl Phys Lett 2007;90(22):223901.
[22] Eghtedari M, Oraevsky A, Copland JA, Kotov NA, Conjusteau A, Motamedi M. High sensitivity in vivo detection of gold nanorods using a laser optoacoustic imaging system. Nano Lett 2007;7(7):1914–8.
[23] Eghtedari M, Liopo AV, Copland JA, Oraevslty AA, Motamedi M. Engineering of hetero-functional gold nanorods for the in vivo molecular targeting of breast cancer cells. Nano Lett 2009;9(1):287–91.
[24] Pan DP, Pramanik M, Senpan A, Yang XM, Song KH, Scott MJ, et al. Molecular photoacoustic tomography with colloidal nanobeacons. Angew Chem Int Ed Engl 2009;48(23):4170–3.
[25] Xiang LZ, Yuan Y, Xing D, Ou ZM, Yang SH, Zhou FF. Photoacoustic molecular imaging with antibody-functionalized single-walled carbon nanotubes for early diagnosis of tumor. J Biomed Opt 2009;14(2):021008.
[26] De La Zerda A, Zavaleta C, Keren S, Vaithilingam S, Bodapati S, Liu Z, et al. Carbon nanotubes as photoacoustic molecular imaging agents in living mice. Nat Nanotechnol 2008;3(9):557–62.
[27] Pramanik M, Song KH, Swierczewska M, Green D, Sitharaman B, Wang LHV. In vivo carbon nanotube-enhanced non-invasive photoacoustic mapping of the sentinel lymph node. Phys Med Biol 2009;54(11):3291–301.
[28] Weissleder R. A clearer vision for in vivo imaging. Nat Biotechnol 2001;19(4):316–7.
[29] Chamberland DL, Agarwal A, Kotov N, Fowlkes JB, Carson PL, Wang X. Photoacoustic tomography of joints aided by an etanercept-conjugated gold nanoparticle contrast agent – an ex vivo preliminary rat study. Nanotechnology 2008;19(9):095101.
[30] Wang B, Yantsen E, Larson T, Karpiouk AB, Sethuraman S, Su JL, et al. Plasmonic intravascular photoacoustic imaging for detection of macrophages in atherosclerotic plaques. Nano Lett 2009;9(6):2212–7.
[31] Li ML, Wang JC, Schwartz JA, Gill-Sharp KL, Stoica G, Wang LHV. In-vivo photoacoustic microscopy of nanoshell extravasation from solid tumor vasculature. J Biomed Opt 2009;14(1):010507.
[32] Sharma P, Brown SC, Bengtsson N, Zhang QZ, Walter GA, Grobmyer SR, et al. Gold-speckled multimodal nanoparticles for noninvasive bioimaging. Chem Mater 2008;20(19):6087–94.
[33] Melancon MP, Lu W, Yang Z, Zhang R, Cheng Z, Elliot AM, et al. In vitro and in vivo targeting of hollow gold nanoshells directed at epidermal growth factor receptor for photothermal ablation therapy. Mol Cancer Ther 2008;7(6):1730–9.
[34] Lu W, Xiong C, Zhang G, Huang Q, Zhang R, Zhang JZ, et al. Targeted photothermal ablation of murine melanomas with melanocyte-stimulating hormone analog-conjugated hollow gold nanospheres. Clin Cancer Res 2009;15(3):876–86.
[35] Schwartzberg AM, Olson TY, Talley CE, Zhang JZ. Synthesis, characterization, and tunable optical properties of hollow gold nanospheres. J Phys Chem B 2006;110(40):19935–44.

[36] El-Sayed MA. Some interesting properties of metals confined in time and nanometer space of different shapes. Acc Chem Res 2001;34(4):257–64.

[37] Mie G. Beiträge zur optik trüber medien, speziell kolloidaler metallösungen. Ann Phys 1908;25(3):377–445.

[38] Stratton JA. Electromagnetic theory. New York: McGraw-Hill; 1941. p. 569.

[39] Kerker M. Scattering of light and other electromagnetic radiation. Physical chemistry. New York: Academic Press; 1997. p. 666.

[40] Xu MH, Wang LHV. Pulsed-microwave-induced thermoacoustic tomography: filtered backprojection in a circular measurement configuration. Med Phys 2002;29(8):1661–9.

[41] Zhang G, Yang Z, Lu W, Zhang R, Huang Q, Tian M, et al. Influence of anchoring ligands and particle size on the colloidal stability and in vivo biodistribution of polyethylene glycol-coated gold nanoparticles in tumor-xenografted mice. Biomaterials 2009;30(10):1928–36.

[42] Connor EE, Mwamuka J, Gole A, Murphy CJ, Wyatt MD. Gold nanoparticles are taken up by human cells but do not cause acute cytotoxicity. Small 2005;1(3):325–7.

[43] Prahl S. Optical absorption of hemoglobin. OMLC. Online 1998. Available from URL:http://omlc.ogi.edu/spectra/hemoglobin/.

[44] Murphy CJ, Gole AM, Stone JW, Sisco PN, Alkilany AM, Goldsmith EC, et al. Gold nanoparticles in biology: beyond toxicity to cellular imaging. Acc Chem Res 2008;41(12):1721–30.

[45] Lu W, Wan J, She ZJ, Jiang XG. Brain delivery property and accelerated blood clearance of cationic albumin conjugated pegylated nanoparticle. J Control Release 2007;118(1):38–53.

[46] Bazile D, Prudhomme C, Bassoullet MT, Marlard M, Spenlehauer G, Veillard M. Stealth Me.PEG-PLA nanoparticles avoid uptake by the mononuclear phago-cytes system. J Pharm Sci 1995;84(4):493–8.

[47] Demoy M, Gibaud S, Andreux JP, Weingarten C, Gouritin B, Couvreur P. Splenic trapping of nanoparticles: complementary approaches for in situ studies. Pharm Res 1997;14(4):463–8.

[48] Liu N, Makino T, Honda G, Muso E, Kita T, Ono T. Suppressive effects of Sairei-to on mesangial proliferation in a rat model of glomerulonephritis. Clin Exp Nephrol 2004;8(3):216–22.